Real-Time Observation of Order-Disorder Transformation of Organic Cations Induced Phase Transition and Anomalous Photoluminescence in Hybrid Perovskites

Bin Yang, Wenmei Ming, Mao-Hua Du, Jong K. Keum, Alexander A. Puretzky, Christopher M. Rouleau, Jinsong Huang, David B. Geohegan, Xiaoping Wang,* and Kai Xiao*

A fundamental understanding of the interplay between the microscopic structure and macroscopic optoelectronic properties of organic-inorganic hybrid perovskite materials is essential to design new materials and improve device performance. However, how exactly the organic cations affect the structural phase transition and optoelectronic properties of the materials is not well understood. Here, real-time, in situ temperature-dependent neutron/X-ray diffraction and photoluminescence (PL) measurements reveal a transformation of the organic cation $CH_3NH_3^+$ from order to disorder with increasing temperature in $CH_3NH_3PbBr_3$ perovskites. The molecular-level order-to-disorder transformation of $CH_3NH_3^+$ not only leads to an anomalous increase in PL intensity, but also results in a multidomain to single-domain structural transition. This discovery establishes the important role that organic cation ordering has in dictating structural order and anomalous optoelectronic phenomenon in hybrid perovskites.

Dr. B. Yang
College of Materials Science and Engineering
Key Laboratory for Micro-Nano Physics and Technology of Hunan Province
Hunan University
Changsha 410082, China
Dr. B. Yang, Dr. J. K. Keum, Dr. A. A. Puretzky, Dr. C. M. Rouleau, Dr. D. B. Geohegan, Dr. K. Xiao
Center for Nanophase Materials Sciences
Oak Ridge National Laboratory
Oak Ridge, TN 37831, USA
E-mail: xiaok@ornl.gov
Dr. W. Ming, Dr. M.-H. Du
Materials Science & Technology Division
Oak Ridge National Laboratory
Oak Ridge, TN 37831, USA
Dr. J. K. Keum, Dr. X. Wang
Neutron Scattering Division
Neutron Sciences Directorate
Oak Ridge National Laboratory
Oak Ridge, TN 37831, USA
E-mail: wangx@ornl.gov
Prof. J. Huang
Department of Mechanical and Materials Engineering
University of Nebraska-Lincoln
Lincoln, NE 68503, USA

Organic–inorganic hybrid perovskites (OIHPs) have emerged as an important group of functional materials for applications in high-performance optoelectronic devices including solar cells,[1,2] light-emitting diodes,[3] photodetectors,[4] and lasers.[5] For example, OIHP solar cells have rapidly progressed to achieve more than 22% power conversion efficiency (PCE) in only about 5 years.[1] The impressive general performance of OIHP devices in these applications is ascribed to a remarkable set of optoelectronic properties,[6] including tunable optical bandgaps,[7] high optical extinction coefficients,[8] high charge carrier mobility,[9,10] and long carrier diffusion length.[6,9] This combination of properties clearly originates from the organic–inorganic hybrid structure[9] in which organic cations in the unit cell are located between eight Pb_6^+ octahedrons. However, understanding how to enhance properties further (e.g., the PCE of OIHP solar cells to the level of monocrystalline silicon solar cells, or close to the theoretical maximum) requires a fundamental understanding of how the OIHP structure impacts the optoelectronic properties.[11] The central question is exactly how the organic cations within the inorganic framework govern the structural and electronic properties of the hybrid materials.

Neutron diffraction offers a unique advantage to study the ordering of organic cations compared to X-ray diffraction because neutrons interact with nuclei, while X-rays interact with atomic orbital electrons so that the scattering intensity on the atoms is proportional to the atomic number. Lead (Pb) in lead halide perovskites is not as dominant for neutrons, as it has bound scattering length of 9.405 fm, which is similar to that of nitrogen (N) (9.36 fm). N has a significantly greater bound coherent scattering length than that of C (6.65 fm). Furthermore, hydrogen (H) is a negative scatterer for neutrons (−3.74 fm). The difference in scattering lengths of the organic component in lead halide perovskites provides high sensitivity to the change in the orientation and reversal of organic cations (e.g., methylammonium (MA) or formamidinium (FA) ions) in hybrid perovskite structure.[12] The TOPAZ single crystal neutron diffractometer at the Spallation Neutron Source uses neutron time-of-flight Laue technique for mapping 3D volumes of
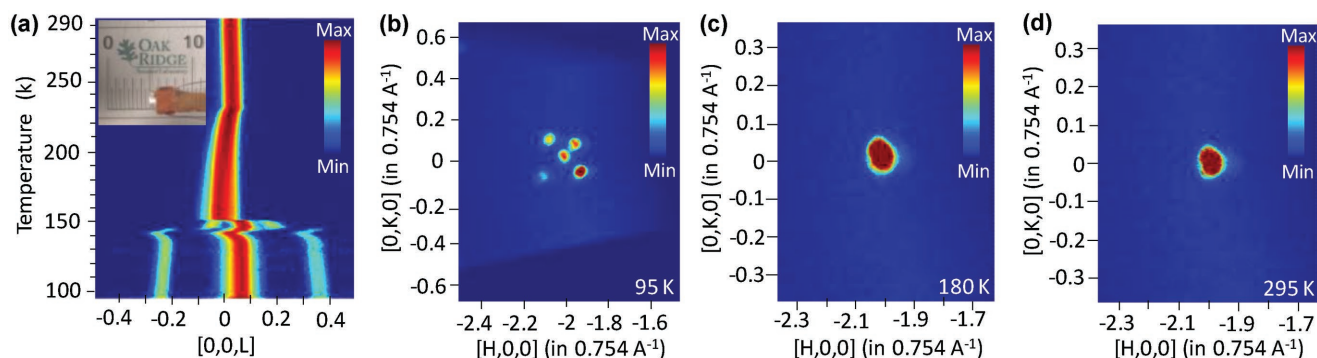
Figure 1. Neutron diffraction of MAPbBr$_3$ single crystals at different temperatures spanning the orthorhombic to tetragonal to cubic phase transition. a) Variable temperature plot showing the change of the (200)$_C$ peak during continuous heating from 95 to 295 K at the rate of 1 K min^{-1}. The (200)$_C$ peak is indexed as the (220)$_T$ peak in the tetragonal I4/mcm phase between 230 and 153 K and the (202)$_O$ peak in the orthorhombic Pnma phase at temperatures below 153 K, respectively. The fluctuation of the (200)$_C$ peak between ≈140 and 155 K is most likely due to the coexistence of the tetragonal and orthorhombic phase. The inset shows a millimeter-size crystal that was used for neutron single crystal diffraction measurements. b–d) 2D scattering profiles of the (200) peak in the (H, K, 0) RLP along the [0, 0, L] direction measured at 95, 180, and 295 K, respectively.

diffraction patterns from a stationary single crystal sample.[13] The 3D neutron diffraction data together with the associated sample parameters are recorded in event mode and are not histogrammed as are those for conventional X-ray experiments, which enables the reconstruction of real-time data from in situ variable temperature neutron diffraction measurements. In addition, in conjunction with complementary X-ray diffraction and photoluminescence (PL) spectroscopic measurements, we can correlate the ordering of organic cations on corresponding observations of perovskite structure and optoelectronic properties.

Methylammonium lead bromide (MAPbBr$_3$) bulk single crystals with millimeter-size (inset of **Figure 1**a) were synthesized by the inverse temperature crystallization method[14] as shown in Figure S1 (Supporting Information). To understand the behavior of the organic moieties MA$^+$ within the inorganic framework, temperature-dependent neutron diffraction measurements on MAPbBr$_3$ single crystals were performed for 95 K ≤ T ≤ 295 K. Neutron diffraction is highly sensitive to the order of organic molecular cations within inorganic frameworks due to the high sensitivity of neutrons to light chemical elements. The cubic Pm-3m (200)$_C$ single crystal peak was monitored as the temperature changed during both cooling (Figure S2, Supporting Information) and heating (Figure 1a) at the same 1 K min^{-1} rate. A movie shows the real-time change of the MAPbBr$_3$ (200)$_C$ peak during continuous heating from 95 to 295 K and cooling from 295 to 95 K at the rate of 1 K min^{-1} (Movie S1, Supporting Information). It should be noted that the (200)$_C$ peak is indexed as (220)$_T$ peak in the tetragonal I4/mcm phase between 230 and 153 K and the (202)$_O$ peak in the orthorhombic Pnma phase at temperatures below 140 K, respectively. Since the change in phase transition temperature between heating and cooling runs was small (less than 2 K), we will focus on the real-time neutron diffraction results from heating. As shown in Figure 1a, the strongly split orthorhombic (202)$_O$ peaks coalesce throughout the entire heating process. The MAPbBr$_3$ single crystal exhibits a peak shift due to the tetragonal distortion during the cubic-to-tetragonal phase transition at 230 K, and peak splitting between 130 and 153 K. There is a pronounced fluctuation in structure observed close to 150 K

that is most likely due to the coexistence of the tetragonal P4/mmm and orthorhombic phases.[15] A strong distortion of the orthorhombic peak at temperatures is also observed above ≈130 K that corresponds to the orthorhombic-to-tetragonal phase transition during heating. The abrupt change that occurs in the temperature range 130–153 K is consistent with the nature of a first-order phase transition. The split peaks merged into a broad (220)$_T$ peak at temperatures above 153 K, corresponding to the formation of the tetragonal I4/mcm phase. Upon heating, the peaks further merge into a single peak above the tetragonal-to-cubic phase transition temperature at 230 K. This behavior is confirmed by slices in reciprocal lattice space at three different phases for the (220)$_T$ peak as shown in Figure 1b–d. A single peak remains at both 180 and 295 K, but splits into five peaks at 95 K. The strongly split orthorhombic (202)$_O$ peaks (>0.3 RLPs) start recombining at ≈131 K and coalesce to the tetragonal (220)$_T$ peak at 153 K.

In order to determine the ordering of the MA$^+$ cations in these different regimes, crystallographic data from neutron diffraction were collected at three temperatures (95, 180, and 295 K). A polyhedral plot in **Figure 2**a shows the ordered MA$^+$ cation in the A site of the Pnma structure deduced from single crystal neutron diffraction data measured at 95 K. This structure was stabilized by the strong trifurcated hydrogen bonds between the N terminal of the MA cation and the bromides on the PbBr$_6$ octahedra (Figures S3 and S4a, and Table S1, Supporting Information). The single-crystal neutron diffraction measurements indicate that the rotational freedom of the MA$^+$ increases with increasing temperature starting from 95 K, whereas a disordered MA$^+$ cation in the I4/mcm structure was revealed from neutron diffraction data measured at 180 K (Figure 2a; Figure S4b, Supporting Information). The MA$^+$ molecular orientation is most likely to begin randomizing near 100 K as shown in Figures 1a and 2b, well before the tilting of the inorganic octahedrons is observed around 130 K, which marks the onset of the phase transition toward the tetragonal structure. It can be concluded from the real-time neutron diffraction study that the transition from multidomain to single-domain in the 100–153 K temperature range (Figure 2b) is associated with the transition of MA$^+$ cations from order to disorder. This observed
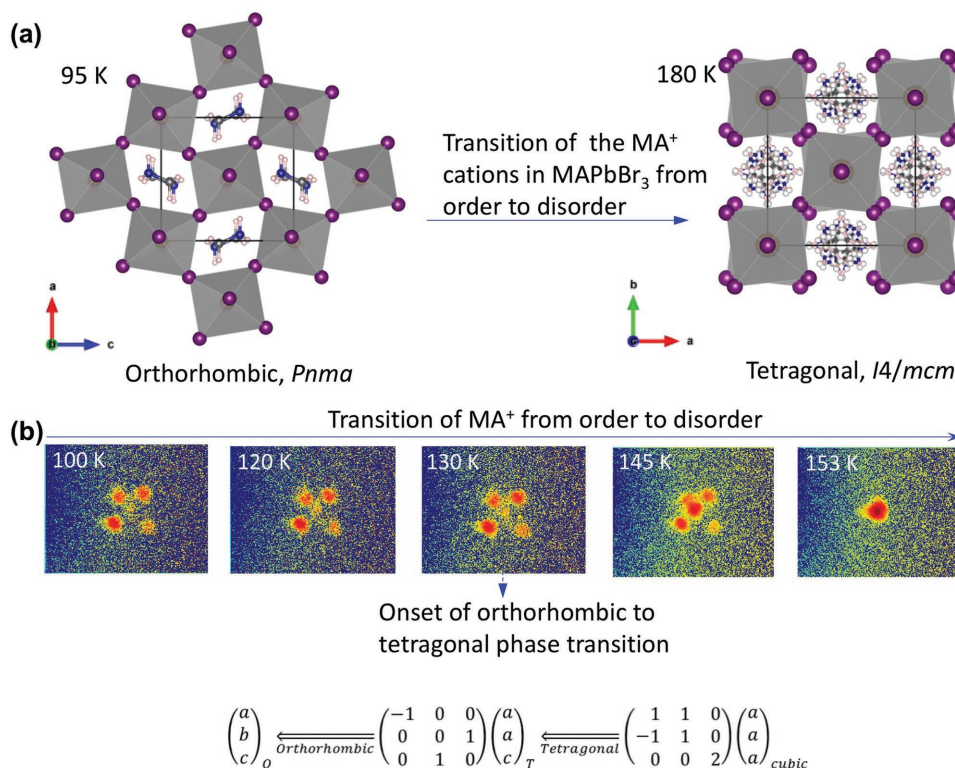
Figure 2. a) Schematic indicating the order-to-disorder transition of $CH_3NH_3^+$ (MA$^+$) cations that results in the structural orthorhombic-to-tetragonal phase transition of the crystal. Left: Polyhedral plot showing the ordered MA$^+$ cation in the A site of the *Pnma* structure from neutron diffraction data measured at 95 K obtained applying the twin law with five-domain structures in neutron structure refinement. Right: Polyhedral plot showing the disordered MA$^+$ cation in the *I4/mcm* structure from neutron diffraction data measured at 180 K. b) The change of the tetragonal (200) peak profile from 100 to 153 K reveals the structural evolution. The [HK0] RPL plot at each temperature used in situ neutron diffraction data binned in ±2 K thickness and viewed against the tetragonal *c* direction. Peak splitting shown in the plots is due to the formation of multidomains in the lower symmetry orthorhombic phase, consistent with reflection twins on the {101} and {121} planes of the *Pnma* structure. The insert in the bottom shows the transformation matrices that map the cubic and tetragonal *c*-axis to the *b*-axis of the orthorhombic cell.

rotational variation of molecular cations MA$^+$ appears to induce the structural orthorhombic-to-tetragonal phase transition, which starts near 130 K, rather than 100 K.

The associated structural phase transition was further characterized using complementary techniques. Temperature-dependent X-ray powder diffraction measurements revealed phase transitions with increasing temperature from orthorhombic to tetragonal to cubic (Figure S5, Supporting Information). In addition, the X-ray reflection peaks of (112)$_O$ and (211)$_T$ observed at 140 K suggested the coexistence of orthorhombic and tetragonal phases (**Figure 3**a). The (211)$_T$ X-ray diffraction (XRD) peak begins to appear at $T = \approx 130$ K, indicating the initial formation of the tetragonal phase at this temperature (Figure 3b). With further increase in temperature, the tetragonal phase (211)$_T$ peak increases, while the (112)$_O$ peak corresponding with the orthorhombic phase decreases, and disappears completely at ≈ 150 K. The real-time, temperature-dependent X-ray observation further demonstrates that a gradual transition from the orthorhombic to tetragonal phase starts at ≈ 130 K and ends at ≈ 150 K, which agrees well with the result from neutron diffraction characterizations. To determine the orthorhombic-to-tetragonal phase transition in the low temperature region, differential scanning calorimetry (DSC) measurements were conducted. Two endothermal peaks were observed at ≈ 145.8 and ≈ 152.6 K

during heating (Figure S6, Supporting Information), which is consistent with the temperature-dependent in situ neutron diffraction observations in Figure 1a that showed a pronounced structure fluctuation between ≈ 140 and ≈ 153 K, from which the coexistence of the tetragonal (P4/mmm) and orthorhombic phases was inferred.[15]

This rotational freedom of the MA$^+$ at $T > 95$ K increases the dielectric screening significantly; for example, free rotation of the MA$^+$ cations has been shown to increase the static dielectric constant from ≈ 30 to $\approx 60–70$.[6,8,16,17] This regional doubling of the static dielectric constant reduces the Coulomb attraction by a charged defect by half, making the defect levels shallower, consequently reducing nonradiative recombination. Moreover, the multidomain structure represents a discontinuity of the octahedral tilt pattern in the orthorhombic phase, which correlates with the orientation of the MA$^+$. Such a discontinuity may create defects at the domain boundaries to release strain. Therefore, the coalescence of multidomains to a single domain (Figure 2b) should cause a reduction in defect density. It is thus hypothesized that during the order-disorder transformation of the organic cations observed as the temperature increases, a reduced nonradiative recombination resulting from increased dielectric screening should result in increased PL that correlates with the reduced defect density
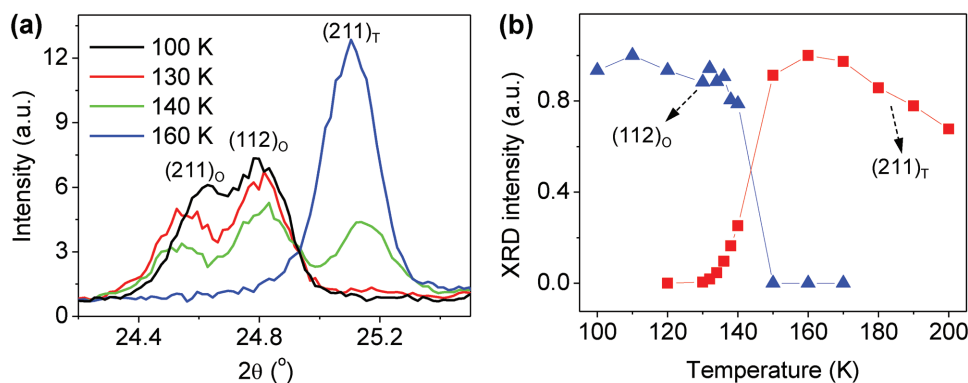
Figure 3. a) XRD patterns at different temperatures, 100 K (dark), 130 K (red), 140 K (green), and 160 K (blue), displaying the variation in $(211)_T$ and $(112)_O$ peaks; additional $(211)_O$ peaks are also exhibited. b) Temperature dependence of integrated X-ray reflection peak intensity of the $(211)_T$ (red squares) of tetragonal phase and $(112)_O$ (blue triangle) of orthorhombic phase reflexes.

during the phase transition from orthorhombic to tetragonal phases.

To test this hypothesis, we acquired the temperature-dependent PL spectra from a $MAPbBr_3$ bulk single crystal (**Figure 4**a). The temperature dependence of the integrated PL peak intensity and peak position from 4 to 200 K are shown in Figure 4b. The PL intensity decreases with increasing temperature as expected in the region labeled "normal" ($T \leq 100$ K and $T \geq 150$ K), which is attributed to nonradiative recombination induced by thermal quenching, a well-established mechanism in semiconductors,[18] whereas the PL intensity is observed to increase with increasing temperature in the region labeled "anomalous" ($\approx$100–150 K). The enhancement in PL intensity results from the reduced nonradiative recombination with increasing temperature, which is due to the increased dielectric screening and the reduction of defect density during transformation from order to disorder of organic cations, consistent with the results obtained from single crystal neutron diffraction measurements. It should be noted that the observed anomalous spike in PL intensity of the $MAPbBr_3$ bulk single crystal at around 130 K (Figure 4a,b) is possibly due to a pronounced structure discontinuity or fluctuation between ordered orthorhombic and disordered tetragonal phases as suggested by the in situ single crystal neutron diffraction and DSC measurements.

Except for an anomalous red shift between 130 and 150 K (Figure 4b) that occurs in the orthorhombic-to-tetragonal

phase transition region, a monotonic blue shift with increasing temperature is typically observed. The blue shift suggests an increase in optical bandgap of $MAPbBr_3$ perovskite single crystals, consistent with other reports for OIHP polycrystalline films,[19,20] but opposite to the observation in typical semiconductors (e.g., Si, GaAs), i.e., the bandgap generally decreases with increasing lattice constant due to the decreasing hybridization (and the decreasing splitting) between the valence and conduction band states.[21] Our calculated bandgap of cubic $MAPbBr_3$ shows a monotonic increase with increasing lattice constant (**Figure 5**b), which agrees with our experimental observation in $MAPbBr_3$ and is also consistent with previous experimental studies[22] and theoretical calculations of other halide perovskites [i.e., $MAPbI_3$ and $CsSnX_3$ (X = Cl, Br, I)].[19,23] To understand this behavior, we specifically calculated the positions of the valence band maximum (VBM), the conduction band minimum (CBM), and the Pb-6s level as a function of the lattice constant. The results clearly show that the hybridization between the Pb-6s level below the valence band and the Br-4p states near the VBM (schematically shown in Figure 5a) is weakened with the expanding lattice, thereby reducing the energy splitting between the Pb-6s level and the VBM (Figure 5b). The lower VBM further reduces the hybridization between the Br-4p states in the valence band and the Pb-6p states in the conduction band, resulting in the rising CBM. Both factors above contribute to the increase of the bandgap as the lattice constant increases.
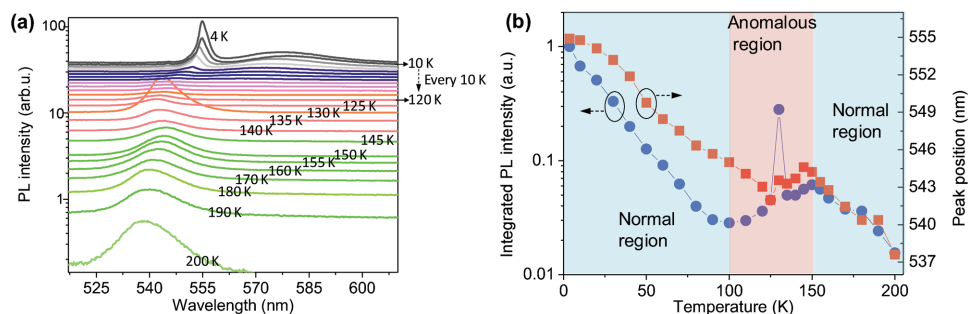

Figure 4. a) Temperature dependence of PL spectra measured from a $MAPbBr_3$ bulk single crystal. b) Temperature dependence of integrated PL peak intensity (blue circles) and PL peak positions (red squares), where light pink region indicates anomalous region (100–150 K) and light blue region shows normal regions (≤100 K and ≥150 K).
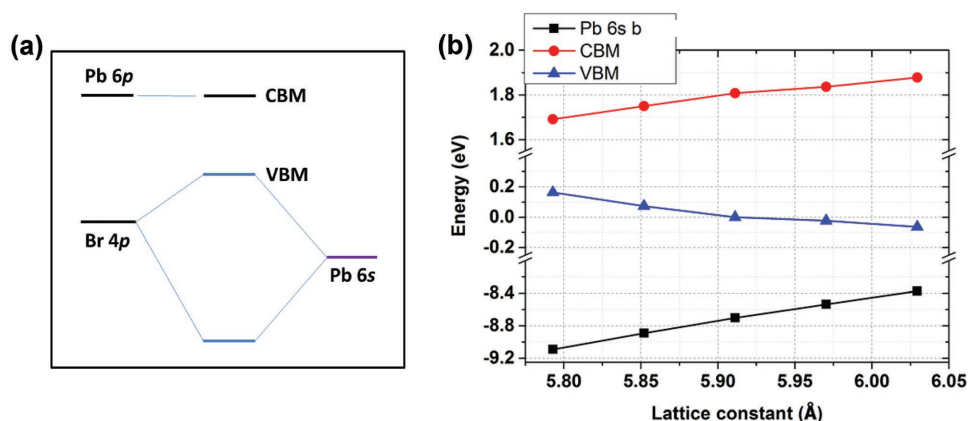
**ADVANCED
SCIENCE NEWS**

www.advancedsciencenews.com

**ADVANCED
MATERIALS**

www.advmat.de

Figure 5. a) Schematic diagram of the hybridization between the Pb 6s and the Br 4p states in MAPbBr$_3$. The Pb 6p states also hybridize with the valence band states, but the hybridization is weak at the band edges; thus, the CBM state appears nearly nonbonding. b) The positions of the CBM, the VBM, and the Pb 6s level (top of the narrow Pb-6s band) at the R point of cubic MAPbBr$_3$ as a function of the lattice constant. The Pb 1s core level is used as the energy reference for the different lattice constants. The VBM calculated at the experimental lattice constant is set to zero.

In addition to the general trend of blue shift of PL peaks with increasing temperature, the PL peak was found to show a slightly but distinct red shift between 130 and 150 K (Figure 4b). The onset (≈130 K) of the anomalous red shift in PL peak is close to the start of the orthorhombic-to-tetragonal phase transition.[17,24] Previous theory calculations suggest that the bandgap of the orthorhombic phase is the largest, followed by those of the tetragonal and the cubic phases at the same volume.[19] Therefore, it is concluded that the phase change induced bandgap variation dominates over the lattice constant induced bandgap variation in the vicinity of phase transitions, leading to the red shift of PL peaks.

It is important to note that the order-disorder transformation of the organic cations has a significant impact on the alignment of the inorganic octahedra. Our neutron diffraction results indicate that the orientation of organic cations began randomizing near 100 K. Correspondingly, the inorganic octahedron tilt pattern in the orthorhombic phase correlates with the orientation of the organic cation CH$_3$NH$_3^+$. However, the order-disorder transformation of the organic cations induces a transformation from tilted inorganic octahedron to nontilted features. This is further indicated by the multidomain structural region, which represents a discontinuity of the octahedron tilting pattern in the orthorhombic phase. Moreover, neutron diffraction measurements revealed the coalescence of multidomain to single-domain structure that correlates with the order-to-disorder transformation of the organic cations. The overall effect of the order-to-disorder transformation of the organic cations on the optoelectronic properties of hybrid perovskites is twofold: one is the increase in static dielectric constant to reduce Coulomb attraction, which makes the defect levels shallower to reduce nonradiative recombination, and the other is the decrease in defect density during the coalescence of multidomain to the single domain, which also should reduce nonradiative recombination. These two factors explain the reduced nonradiative recombination resulting in the enhanced PL intensity in the anomalous region between 100 and 150 K during the phase transition from orthorhombic to tetragonal phases.

In conclusion, real-time neutron diffraction studies revealed the transformation of MA$^+$ cations from order to disorder between 100 and 153 K, which significantly alters the tilt of the inorganic octahedra, corresponding to the induced transitions from orthorhombic to tetragonal phases and from multidomain to single-domain structure. This reduction in defect density, along with the reduction in dielectric screening caused by increasing disorder of the MA$^+$ cations with increasing temperature reduces nonradiative recombination to yield the observed anomalous PL peak intensity. This study enhances the fundamental understanding between microscopic molecular structure and macroscopic optoelectronic performance in OIHPs, essential for the design of new OIHP materials to improve device performance.

Experimental Section

Bulk Single Crystal Growth: The CH$_3$NH$_3$PbBr$_3$ (MAPbBr$_3$) bulk single crystals were grown as following reported methods with modifications.[14] PbBr$_2$ and CH$_3$NH$_3$Br (MABr) powders with equal molar ratio were dissolved in dimethylformamide solvent to make total molar concentration solution of 0.8 M. PbBr$_2$ and MABr were purchased from Sigma-Aldrich and 1-Material, respectively. They were used as received. A vial with 1.25 mL solution was placed in an 80 °C oil bath, as shown in Figure S1 (Supporting Information). After about 3 h of growth, ≈2 mm × 3 mm × 3 mm shiny bulk crystals were obtained. The crystal size can be tailored for neutron diffraction characterizations by changing the growth time. The crystal growth was conducted in ambient air.

Single Crystal Neutron Diffraction: Variable temperature experiment for MAPbBr$_3$ was performed on the TOPAZ single crystal diffractometer at the Spallation Neutron Source, Oak Ridge National Laboratory.[25] Sample temperature control used Oxford Cryosystems Cryostream Plus 700 with an LN$_2$-gasflow setup. A block-shaped hydrogenated single crystal of MAPbBr$_3$ with the dimensions of 1.00 × 1.75 × 1.95 mm^3 was mounted onto the tip of a MiTeGen loop with Super Glue, and transferred to the TOPAZ goniometer for data collection. TOPAZ is a neutron wavelength-resolved, or time-of-flight Laue diffractometer with extensive area-detector coverage capable of 3D Q-space mapping from a stationary single crystal at predefined setting angles. Single-crystal neutron diffraction data are recorded in event mode, in which a continuous 3D volume of reciprocal space can be measured while the

change in sample temperature is monitored and recorded in real time. Using the initial orientation matrix obtained at room temperature, the (2 0 0) peak in the cubic $P\,m$-$3m$ cell was placed on a forward scattering detector with the aid of CrystalPlan software.[26] The single crystal sample was then cooled to 95 K at a ramp rate of 1 K min^{-1}. The sample was then heated from 95 to 300 K at the same ramping rate of 1 K min^{-1} for in situ data collection during sample heating and cooling. Neutron data reduction used the Mantid software.[27] The plots shown in Figure 1b–d used data measured at a longer time interval of 40 min. at each of the sample temperatures of 95, 180, and 295 K, separately. The graphics shown in Figures 1 and 2, and in Figure S2, and Movie S1 in the Supporting Information were generated using the Slice Viewer program available in Mantid.[27] In addition to temperature ramping, full single crystal diffraction datasets for MAPbBr$_3$ at 295, 180, and 95 K were also collected. The integrated raw Bragg intensities were obtained using the 3D ellipsoidal Q-space integration in accordance with previously reported methods.[28] Data reduction including neutron TOF spectrum Lorentz and detector efficiency corrections was carried out with the ANVRED3 program.[29] The *Pnma* data at 95 K were twinned and the reflections were grouped into five domains in HKLF5 format accordingly using the twin law from TwinRotMat in Platon program[30] for structure refinement. Twinning was detected for the *I4/mcm* dataset collected at 180 K due to tetragonal distortions into three domains from symmetry lowering of the idealized cubic *Pm-3m* structure, although no peak splitting was observed. Neutron structure refinements used the SHELX 2014 program.[31] Positions of hydrogen atoms on the disordered MA cation were modeled with the HFIX 137 constraint in SHELX, which allows for free rotation of the −CH$_3$/−NH$_3$ groups along the C−N bond, but keeps the "idealized" C−H/N−H bond distances and tetrahedral angles fixed at default values. VESTA program was used for plot and visualization of the neutron structure.[32]

Temperature-Dependent X-ray Diffraction: Temperature-dependent cryogenic XRD measurements were conducted using a powder X-ray diffractometer (PANAlytical X'Pert MPD Pro) with Cu-Kα radiation (λ = 1.54050 Å), which is equipped with an Oxford Phenix cryogenic XRD stage. The step size and scan rate for each measurement were 0.0167113° and 0.107815° s^{-1}, respectively. A millimeter size bulk single crystal was grinded into a fine powder for temperature-dependent XRD experiment. The cryogenic temperature was controlled by helium compressor at a ramp rate of 2 K min^{-1}. Figure S5 (Supporting Information) was acquired from heating process.

Low-Temperature Differential Scanning Calorimetry: The DSC measurements were conducted to determine the orthorhombic-to-tetragonal phase transition in the low temperature range by Netzsch DSC214. The mass of the sample (fresh MAPbBr$_3$ bulk single crystal) was 10.03 mg. The sample was cooled with liquid nitrogen to achieve a temperature as low as 90 K. DSC curves during heating and cooling were acquired at a ramp rate of 2 K min^{-1}. The intersection of the tangent of the arising part of the peak and the baseline of the DSC curve was applied to determine phase transition temperatures.

Temperature-Dependent Photoluminescence: The PL spectra were measured in a custom-built micro-PL setup. The PL was excited with a continuous wave diode laser (Ondax, 405 nm, 40 mW) through an upright microscope using a 50x-long working distance objective with numeric aperture = 0.5 (beam spot ≈1.5 μm). The typical incident laser power on a sample was maintained at ≈2 μW. The PL light was analyzed by a spectrometer (Spectra Pro 2300i, Acton, f = 0.3 m) that was coupled to the microscope and equipped with 150, 600, and 1800 groves mm^{-1} gratings and a CCD camera (Pixis 256BR, Princeton Instruments). The typical acquisition times were varied from 0.5 to 5 s depending on the PL intensity. The low-temperature PL spectra were measured using a liquid He-cryostat (MicrostatHiResII, Oxford Instruments) with a temperature controller (MercuryiT, Oxford Instruments) that allowed precise temperature control from 4 to 300 K. The cryostat was mounted on a motorized XY microscope stage (Marzhauser). The cryostat was evacuated to the base pressure of 7×10^{-7} mbar prior to cool down.

Density Functional Theory Calculations: The calculations were based on density functional theory with plane-wave basis as implemented in the VASP code.[33] The projector augmented wave method was used to describe the interaction between ions and electrons.[34] Perdew–Burke–Ernzerhof (PBE) functional[35] was adopted to approximate the exchange–correlation interaction. The lattice constants of MAPbBr$_3$ measured by neutron scattering measurements were used: a = 7.986 Å, b = 11.859 Å, and c = 8.582 Å for the orthorhombic phase at 95 K; a = b = 8.3491 Å and c = 11.8202 Å for the tetragonal phase at 180 K (present work); a = b = c = 5.912 Å for the cubic phase at 225 K (ref. [13]).[36] The kinetic energy cutoff of 400 eV was used. For k-point sampling in the reciprocal space, 4 × 2 × 4, 4 × 4 × 2, and 6 × 6 × 6 k-point meshes for the primitive cells of the orthorhombic, the tetragonal, and the cubic phases, respectively, were used. The atomic positions were fully relaxed until the residual forces were less than 0.02 eV Å^{-1}. Spin–orbit coupling (SOC) was not included in the calculations because, in this study, the focus was on the differences between various energy levels, which are insensitive to the SOC.

In the calculations of the lattice constant dependence of the CBM, the VBM, and the Pb-6s state, the cubic phase was used and the Pb 1s core level was used as the reference energy level. The MA molecular orientations are random in the cubic phase. However, in the calculations, the molecular orientation had to be fixed. It was chosen to align the MA molecules along the [111] direction because such molecular orientation causes least structural distortion from the perfect cubic perovskite structure compared to the molecular orientations along the [100] and [110] directions. The structural distortion may induce additional bandgap change and thus was avoided.

Crystallographic data *CCDC No. 1533441(295K), 1533443(180 K), and 1533442 (95 K)* contain the supplementary crystallographic data for the neutron structures as shown in this paper. These data can be obtained free of charge from The Cambridge Crystallographic Data Centre via www.ccdc.cam.ac.uk/data_request/cif.

Supporting Information

Supporting Information is available from the Wiley Online Library or from the author.

Acknowledgements

Conflict of Interest

The authors declare no conflict of interest.

Keywords

[1] a) F. Bella, G. Griffini, J.-P. Correa-Baena, G. Saracco, M. Grätzel, A. Hagfeldt, S. Turri, C. Gerbaldi, *Science* **2016**, *354*, 203; b) G. E. Eperon, T. Leijtens, K. A. Bush, R. Prasanna, T. Green, J. T.-W. Wang, D. P. McMeekin, G. Volonakis, R. L. Milot, R. May, A. Palmstrom, D. J. Slotcavage, R. A. Belisle, J. B. Patel, E. S. Parrott, R. J. Sutton, W. Ma, F. Moghadam, B. Conings, A. Babayigit, H.-G. Boyen, S. Bent, F. Giustino, L. M. Herz, M. B. Johnston, M. D. McGehee, H. J. Snaith, *Science* **2016**, *354*, 861; c) N. J. Jeon, J. H. Noh, W. S. Yang, Y. C. Kim, S. Ryu, J. Seo, S. I. Seok, *Nature* **2015**, *517*, 476.

[2] H. Zhou, Q. Chen, G. Li, S. Luo, T.-B. Song, H.-S. Duan, Z. Hong, J. You, Y. Liu, Y. Yang, *Science* **2014**, *345*, 542.

[3] a) H. Cho, S.-H. Jeong, M.-H. Park, Y.-H. Kim, C. Wolf, C.-L. Lee, J. H. Heo, A. Sadhanala, N. Myoung, S. Yoo, *Science* **2015**, *350*, 1222; b) M. Yuan, L. N. Quan, R. Comin, G. Walters, R. Sabatini, O. Voznyy, S. Hoogland, Y. Zhao, E. M. Beauregard, P. Kanjanaboos, Z. Lu, D. H. Kim, E. H. Sargent, *Nat. Nanotechnol.* **2016**, *11*, 872.

[4] Y. Fang, J. Huang, *Adv. Mater.* **2015**, *27*, 2804.

[5] a) A. Fu, P. Yang, *Nat. Mater.* **2015**, *14*, 557; b) H. Zhu, Y. Fu, F. Meng, X. Wu, Z. Gong, Q. Ding, M. V. Gustafsson, M. T. Trinh, S. Jin, X. Zhu, *Nat. Mater.* **2015**, *14*, 636.

[6] M. A. Green, A. Ho-Baillie, H. J. Snaith, *Nat. Photonics* **2014**, *8*, 506.

[7] T. J. Jacobsson, J.-P. Correa-Baena, M. Pazoki, M. Saliba, K. Schenk, M. Grätzel, A. Hagfeldt, *Energy Environ. Sci.* **2016**, *9*, 1706.

[8] Q. Lin, A. Armin, R. C. R. Nagiri, P. L. Burn, P. Meredith, *Nat. Photonics* **2015**, *9*, 106.

[9] M.-H. Du, *J. Mater. Chem. A* **2014**, *2*, 9091.

[10] J. Chang, J. Xiao, Z. Lin, H. Zhu, Q.-H. Xu, K. Zeng, Y. Hao, J. Ouyang, *J. Mater. Chem. A* **2016**, *4*, 17464.

[11] a) W. Q. Liao, Y. Zhang, C. L. Hu, J. G. Mao, H. Y. Ye, P. F. Li, S. D. Huang, R. G. Xiong, *Nat. Commun.* **2015**, *6*, 7338; b) Y. M. You, W. Q. Liao, D. Zhao, H. Y. Ye, Y. Zhang, Q. Zhou, X. Niu, J. Wang, P. F. Li, D. W. Fu, Z. Wang, S. Gao, K. Yang, J. M. Liu, J. Li, Y. Yan, R. G. Xiong, *Science* **2017**, *357*, 306; c) Y. Zhang, W.-Q. Liao, D.-W. Fu, H.-Y. Ye, C.-M. Liu, Z.-N. Chen, R.-G. Xiong, *Adv. Mater.* **2015**, *27*, 3942.

[12] a) T. Chen, W. L. Chen, B. J. Foley, J. Lee, J. P. C. Ruff, J. Y. P. Ko, C. M. Brown, L. W. Harriger, D. Zhang, C. Park, M. Yoon, Y.-M. Chang, J. J. Choi, S.-H. Lee, *Proc. Natl. Acad. Sci. USA* **2017**, *114*, 7519; b) T. Chen, B. J. Foley, B. Ipek, M. Tyagi, J. R. Copley, C. M. Brown, J. J. Choi, S.-H. Lee, *Phys. Chem. Chem. Phys.* **2015**, *17*, 31278; c) D. H. Fabini, T. A. Siaw, C. C. Stoumpos, G. Laurita, D. Olds, K. Page, J. G. Hu, M. G. Kanatzidis, S. Han, R. Seshadri, *J. Am. Chem. Soc.* **2017**, *139*, 16875.

[13] T. M. Michels-Clark, A. T. Savici, V. E. Lynch, X. Wang, C. M. Hoffmann, *J. Appl. Crystallogr.* **2016**, *49*, 497.

[14] M. I. Saidaminov, A. L. Abdelhady, B. Murali, E. Alarousu, V. M. Burlakov, W. Peng, I. Dursun, L. Wang, Y. He, G. Maculan, A. Goriely, T. Wu, O. F. Mohammed, O. M. Bakr, *Nat. Commun.* **2015**, *6*, 7586.

[15] a) N. Onoda-Yamamuro, O. Yamamuro, T. Matsuo, H. Suga, *J. Phys. Chem. Solids* **1992**, *53*, 277; b) A. Poglitsch, D. Weber, *J. Chem. Phys.* **1987**, *87*, 6373; c) T. Yin, Y. Fang, X. Fan, B. Zhang, J. L. Kuo, T. J. White, G. M. Chow, J. Yan, Z. X. Shen, *Chem. Mater.* **2017**, *29*, 5974.

[16] J. Even, L. Pedesseau, C. Katan, *J. Phys. Chem. C* **2014**, *118*, 11566.

[17] N. Onoda-Yamamuro, T. Matsuo, H. Suga, *J. Phys. Chem. Solids* **1992**, *53*, 935.

[18] S. Poncé, Y. Jia, M. Giantomassi, M. Mikami, X. Gonze, *J. Phys. Chem. C* **2016**, *120*, 4040.

[19] M. I. Dar, G. Jacopin, S. Meloni, A. Mattoni, N. Arora, A. Boziki, S. M. Zakeeruddin, U. Rothlisberger, M. Grätzel, *Sci. Adv.* **2016**, *2*, e1601156.

[20] a) A. D. Wright, C. Verdi, R. L. Milot, G. E. Eperon, M. A. Pérez-Osorio, H. J. Snaith, F. Giustino, M. B. Johnston, L. M. Herz, *Nat. Commun.* **2016**, *7*, 11755; b) K. Wu, A. Bera, C. Ma, Y. Du, Y. Yang, L. Li, T. Wu, *Phys. Chem. Chem. Phys.* **2014**, *16*, 22476.

[21] Y. P. Varshni, *Physica* **1967**, *34*, 149.

[22] B. J. Foley, D. L. Marlowe, K. Sun, W. A. Saidi, L. Scudiero, M. C. Gupta, J. J. Choi, *Appl. Phys. Lett.* **2015**, *106*, 243904.

[23] a) L.-Y. Huang, W. R. Lambrecht, *Phys. Rev. B* **2013**, *88*, 165203; b) I. Borriello, G. Cantele, D. Ninno, *Phys. Rev. B* **2008**, *77*, 235214.

[24] N. Onoda-Yamamuro, T. Matsuo, H. Suga, *J. Phys. Chem. Solids* **1990**, *51*, 1383.

[25] G. Jogl, X. Wang, S. A. Mason, A. Kovalevsky, M. Mustyakimov, Z. Fisher, C. Hoffman, C. Kratky, P. Langan, *Acta Crystallogr., Sect. D: Biol. Crystallogr.* **2011**, *67*, 584.

[26] J. Zikovsky, P. F. Peterson, X. P. Wang, M. Frost, C. Hoffmann, *J. Appl. Crystallogr.* **2011**, *44*, 418.

[27] O. Arnold, J.-C. Bilheux, J. M. Borreguero, A. Buts, S. I. Campbell, L. Chapon, M. Doucet, N. Draper, R. F. Leal, M. A. Gigg, V. E. Lynch, A. Markvardsen, D. J. Mikkelson, R. L. Mikkelson, R. Miller, K. Palmen, P. Parker, G. Passos, T. G. Perring, P. F. Peterson, S. Ren, M. A. Reuter, A. T. Savici, J. W. Taylor, R. J. Taylor, R. Tolchenov, W. Zhou, J. Zikovsky, *Nucl. Instrum. Methods Phys. Res., Sect. A* **2014**, *764*, 156.

[28] A. J. Schultz, M. R. V. Jørgensen, X. Wang, R. L. Mikkelson, D. J. Mikkelson, V. E. Lynch, P. F. Peterson, M. L. Green, C. M. Hoffmann, *J. Appl. Crystallogr.* **2014**, *47*, 915.

[29] A. J. Schultz, K. Srinivasan, R. G. Teller, J. M. Williams, C. M. Lukehart, *J. Am. Chem. Soc.* **1984**, *106*, 999.

[30] A. L. Spek, *Acta Crystallogr., Sect. D: Biol. Crystallogr.* **2009**, *65*, 148.

[31] G. M. Sheldrick, *Acta Crystallogr., Sect. C: Struct. Chem.* **2015**, *71*, 3.

[32] K. Momma, F. Izumi, *J. Appl. Crystallogr.* **2011**, *44*, 1272.

[33] G. Kresse, J. Furthmüller, *Phys. Rev. B* **1996**, *54*, 11169.

[34] G. Kresse, D. Joubert, *Phys. Rev. B* **1999**, *59*, 1758.

[35] J. P. Perdew, K. Burke, M. Ernzerhof, *Phys. Rev. Lett.* **1996**, *77*, 3865.

[36] I. Swainson, R. Hammond, C. Soulliere, O. Knop, W. Massa, *J. Solid State Chem.* **2003**, *176*, 97.